Tribochemistry dependence of $Ni_{62}Nb_{33}Zr_5$ bulk metallic glass on the Cr content of steel counterparts

Guillaume Colas [1*], María del Carmen Marco de Lucas [2], Luc Imhoff [2], Olivier Heintz [2], Rémi Daudin [3], Alexis Lenain [4], Sébastien Gravier [4], Pierre-Henri Cornuault [1]

[1] Univ. Franche-Comté, CNRS, institut FEMTO-ST, F-25000 Besançon, France
[2] Laboratoire Interdisciplinaire Carnot de Bourgogne (ICB), UMR6303 CNRS-Université de Bourgogne, 9 avenue Alain Savary, BP 47870, 21078 Dijon Cedex, France
[3] University of Grenoble Alpes, CNRS, SIMaP, 38000, Grenoble, France
[4] Vulkam Inc. Amorphous metal micro casting, 38610 Gières, France

*corresponding author: Guillaume.colas@femto-st.fr

Abstract

Recent literature showed that Bulk Metallic Glasses can demonstrate repeatable tribological response, and that it might be controlled through a careful selection of the sliding counterpart's composition. The present study focuses on the effect of Cr content of a steel ball sliding over a $Ni_{62}Nb_{33}Zr_5$ BMG. Three different steels were chosen (C90, 100Cr6, and X105CrMo17) because they demonstrate similar constitutive elements, similar mechanical properties, but different Cr contents. Increasing Cr content resulted in an increase of friction coefficient from 0.13 to 0.85 while maintaining extremely low wear. In depth chemical analysis showed that increasing Cr content favors the loss of the ductile Nb_2O_5 of protective $FeNbO_4$, and NiNb-oxide to the benefit of NiCrO, $CrNbO_4$, NiFe-oxides, and Cr(VI) oxide.

Keywords: metallic glass, tribology, tribochemistry

---

1 Introduction

Metallic glasses (MG), also known as amorphous metallic alloys (AMA), were first obtained as ribbons in the 60's by quenching an AuSi melt [1]. They can now be produced in bulk form (BMG) through injection molding [2–4], or through additive manufacturing [5], which both requires specific processing conditions (inert atmosphere, dedicated compositions, and controlled cooling rates) to result in a metallic material deprived of crystalline structure. Therefore, they can offer efficient alternatives in micro-devices [3,6,7]. Indeed, the lack of crystallization leads to isochore solidification that demonstrates insignificant shrinkage, and very low surface roughness. Very small net-shaped BMG parts of various compositions can be produced, particularly by injection moulding. An outstanding feature of BMG is that despite having 'no microstructure' they exhibit among the highest product of yield stress and fracture toughness of any known material [8,9]. They also have low Young's modulus, large elastic strain limit (~1.9%), high hardness and are corrosion resistant.

The novel properties of BMGs have naturally led to their interest in designing parts subjected to tribological contact, and consequently to friction and wear. This interest is now growing due to the need to miniaturize mechanical systems in many sectors, leading to more and more stringent sliding and rolling speeds and contact pressures. Tribological studies of the last two decades showed that: (1) The wear resistance of BMGs as compared to crystalline alloys has been highly debated [3,10–14] (2) The friction coefficients measured on BMGs are generally very high (0.4 to 1) [10,11,15,16] although a recent study showed friction coefficient as low as 0.1 [17,18]. (3) The tribological mechanisms observed also vary a lot according to the friction conditions (speed, pressure, geometry, kinematics...) [3,10,13,17]. Nonetheless recent studies conducted respectively at the nanoscale [19], and at the macroscale [17,18], showed that BMGs are very sensitive to the nature of the counter part. That, hence suggest that it could be possible to finely control friction and wear of BMG by carefully selecting the sliding counterparts based on its elemental composition.

The family of metallic glasses compositions is very large [8], among which a large group have been identified as relevant for applications that are of interest in this study, i.e. tribological application in which sliding occurs. Those alloys are mostly based on compositions where Cu, Zr, Ni, Fe, or Ti are the main element in weight% [3,13,20]. The literature shows that Cu- and Ni-based alloys demonstrate among the lowest volume loss on tribometer test [13,17] while Ni and Zr-based alloys exhibit extended wear lives in gear applications [3,20]. Ni-based alloys particularly demonstrated an extension of micro-gear wear life by a factor of 313 as compared to common SK-steel [3].

It has been showed in a previous work [17] that, at low contact pressure, $Ni_{62}Nb_{33}Zr_5$ BMG offered long lasting low friction (0.1) and extremely low wear when sliding against 100Cr6. However, at high contact pressure, friction increased by nine-fold (0.9), and wear volume by seven-fold making wear still extremely low (by 6 times) as compared to the other test BMGs. The analysis of the elemental composition of the friction track and 3rd bodies showed that in the high friction case, Cr was detected in the friction track in a significant amount. It was hence presumed that the Cr contained in the steel counterpart was at the origin of the high friction, and that higher contact pressure led to easier diffusion and transfer of Cr towards the friction track. The present paper consequently aims at verifying the assumption that the Cr content of a steel sliding body may indeed be used to master the friction coefficient of $Ni_{62}Nb_{33}Zr_5$ BMG. Results eventually demonstrated that such a control is indeed possible which confirmed a new route towards mastering friction and wear of $Ni_{62}Nb_{33}Zr_5$ BMG by selecting the counterpart material based on its Cr content.

2 Materials and Methods

2.1 Materials

The present study focuses on one Ni-based ($Ni_{62}Nb_{33}Zr_5$), and three different steels compositions (C90, 100Cr6, and X105CrMo17) as sliding counter materials. Those alloys were chosen based on their respective content in Cr, and both on their relatively close content in C and additional micro-alloying elements. The compositions of the steels are listed in Table 1, from the highest to the lowest Cr content in the material. The Vickers hardness of each steel, over 5 measurements with a load of 5 kg, is 883±21 HV for C90, 807±12 HV for 100Cr6, and 724±24 HV for X105CrMo17.

Steel	Fe	C	Cr	Mo	Mn	Si	Ni	Cu
C90	*Balance*	0.9	-	0.6	1	0.6	-	-
100Cr6	*Balance*	0.95-1.05	1.40-1.65	-	0.25-0.45	0.15-0.35	0.30 max	0.20 max
X105CrMo17	*Balance*	0.95-1.20	16.00-18.00	0.75 max	1.00 max	1.00 max	-	-

Table 1 – Chemical composition (wt%) of the steels used as counterparts.

Regarding the $Ni_{62}Nb_{33}Zr_5$ fabrication, the primary alloy was produced by arc-melting (T>2500 °C) bulk fragments of the base elements of high purity (>99.9%) under argon atmosphere using a Ti getter for detection of any detrimental contamination traces. The primary alloy was melted at least five times to ensure a high quality of the chemical homogeneity and was subsequently melted again and injected into a dedicated mold to produce a plate-shaped sample ($15\times8\times1$ mm^3). The crystal structure of the plate was analyzed by X-ray diffraction measurements using a Rigaku smartlab equipment with Cu-Kα radiation (cf. Supplementary Material Figure S1). Young's modulus, and Poisson's ratio of the BMG, measured using an Olympus S35 ultrasonic echoes apparatus, are 153±4 GPa and 0.33, respectively. Similar mechanical behavior was found in [15] for Ni-based BMGs having chemical composition close to the one studied herein. The yield strength of the material has been measured at 3060±120 MPa (cf. Figure

S2) Vickers hardness over 10 measurements with a load of 1 kg, is 798±8 HV for $Ni_{62}Nb_{33}Zr_5$. The BMG hence exhibits similar hardness to the 100Cr6 but it is harder than the X105CrMo17 and softer than the C90.

2.2 Friction tests

Friction and wear properties of the $Ni_{62}Nb_{33}Zr_5$ BMG plate were tested under dry sliding condition against 5 mm diameter C90, 100Cr6, and X105CrMo17 steel ball counterpart. Before experiments, both balls and plate were ultrasonically cleaned in absolute ethanol during 5 min and then dried in air. Reciprocating ball-on-plate friction tests were performed at room temperature (22 ± 2 °C) and in ambient air. The displacement stroke is ±1 mm (2mm maximum amplitude), and the reciprocating frequency is 1 Hz, which results a sliding speed of 4 mm/s. The duration of the tests was set at 10,000 backward-and-forward friction cycles, which results in a 40 m total sliding distance. A constant normal force $F_N = 0.25$ N was applied throughout the test using dead loads, that corresponds to 420 MPa of maximum Hertz initial contact pressure (calculated as in [17]). Such moderately high contact pressure is chosen as it lies in between low and high contact pressures from the study that questioned the role of Cr in $Ni_{62}Nb_{33}Zr_5$ tribological response [17]. The purpose is to complement previous results, and to induce wear mechanisms more moderately to study the underlying tribochemical mechanisms. Steel balls all have the same mechanical properties ($E_1 = 210$ GPa and $\nu_1 = 0.29$). Several tests per configuration were conducted to assess results reproducibility.

Throughout each friction test, the relative displacement of the ball h and the friction force F_T were measured thanks to LVDT and piezoelectric sensors, respectively. Both signals were recorded with a 512 Hz sampling frequency. The friction coefficient μ related to the whole friction cycle was calculated from an energetic point of view using (1), where Δh_0 is the distance (close to 2 mm) between the two extreme positions of the friction track where $F_T = 0$.

$$\mu = \frac{1}{2\,\Delta h_0} \int \left| \frac{F_T}{F_N} \right| dh \qquad (1)$$

This approach has the advantage to circumvent the local increases of the friction coefficient F_T/F_N that usually occur at the friction track extremities. Nonetheless, interest is also given to the stability of the friction over the track. Standard deviation of the friction coefficient is hence calculated over 80% of the track length, data at extremities is not being considered.

2.3 Post-test analyses

Morphological and topographical analyses: After friction test, observations of all friction scars were carried out using a Keyence VHX-6000 digital microscope. Surface topography characterization of every friction tracks (balls and plates) were also performed using a variable focus optical microscope (InfiniteFocus, Alicona Imaging GmbH). The three-dimension surface topography collected were then analysed with a dedicated home-made image processing software in order to characterize damages and wear volumes of the friction scars. In this study, wear was defined as a lost volume of matter, meaning that phenomena such like material transfer can eventually lead to negative wear values (matter addition). Volume calculation is described in a previous study [17]. Friction track and 3rd body morphologies are also analyzed in more details by Scanning Electron Microscopy (SEM). SEM imaging was performed on a Zeiss ultra 55 MEG-FEG operated at 5 kV (Everhart-Thornley detector),

Chemical analysis: in depth chemical analysis of the friction track was conducted with complementary analysis tools. Local but deep (few hundreds nanometer thick layer) elemental composition of the materials was studied with Energy Dispersive Spectroscopy (EDS), which is combined with the SEM.

EDS analyses were conducted at 15 kV and 10 kV with a Bruker SD detector. Less local but still deep, Raman spectroscopy was conducted to identify if specific oxides are created during friction. Raman spectra were made using a Renishaw inVia micro-Raman spectrometer in backscattering configuration. The spectra were recorded using 532 and 633 nm wavelength lasers as excitation sources. The laser power was about 0.5 mW to avoid the damage of the samples, mainly the 3rd bodies. Some materials are not demonstrating any Raman response, and some are very sensitive to local rise of temperature due to laser interaction, X-ray Photoelectron Spectroscopy (XPS) has hence been performed.

The oxidation state of the elements as well as the metal–oxide interaction were monitored using X-ray photoelectron spectroscopy (XPS) measurements. The XPS spectra were acquired with a PHI 5000 Versaprobe apparatus with an Al Kα1 radiation source (energy = 1486.7 eV, accelerating voltage = 15 kV, power = 50 W, and spot size diameter = 200 µm). Pass energies of 187 eV and 58.7 eV were used for survey spectra and high-resolution windows, respectively. Casa XPS software is used for data treatment. All measurements are calibrated with adventitious carbon (C1s at 184.8 eV). XPS is complementary to EDS and Raman as the analysis is conducted over a large area (due to the spot size) but over only few nanometers in depth. In our particular case study, Cr signal happened to be hidden by C related signal, Nano Secondary Ion Mass Spectrometry (Nano-SIMS) has consequently been performed.

The measurements were performed using a PHI nanoTOF II working with Bi_3^{2+} ions (30 keV). The analyzed area is a square of 200×200 μm^2. Although destructive due to the heavy ion bombardment of the surface, Nano-SIMS provides information on the chemical and isotopic composition of the surface over a depth of around two atomic layers. It is also local analysis, more local than XPS and Raman for example. The lateral resolution is high thanks to a spot size of around 100nm of diameter. Mapping of the friction track composition have been performed, and intensities of secondary ions of region of interests (ROI) have also been extracted to compare the repartition of the different 3rd bodies encountered and the pristine BMG surface. Intensities (counts on the spectrum) are normalized to allow comparisons between the different spectra. In negative detection mode, intensity of each spectrum is normalized by the total intensity of the spectrum itself. In positive detection mode, normalization is done by dividing the intensity by the [total intensity minus the intensities relative to Na^+ (masses 23 to 24), Ca^+ (masses 37 to 44), Cs^+ (masses 132 to 134)].

3 Results and discussion

3.1 Friction coefficients and wear analysis

The friction coefficient variations over the total test duration (Figure 1, top plot) show very good reproducibility of the tribological response of each friction pair (X105CrMo17/BMG, 100Cr6/BMG, and C90/BMG). Reproducibility is even observed during the very first cycles of friction (cf. Figure S3 in Supplementary Information). After only a few tens of friction cycles, the X105CrMo17/BMG friction pair demonstrates rapid increase of friction coefficient until it reaches very high friction coefficient μ close to 0.8. In contrast, the two other friction pairs exhibit extremely low and stable friction throughout the test. The mean friction coefficients referring to the overall sliding distance recorded are 0.15 and 0.12 when the BMG is rubbed against the 100Cr6 ball and the C90 ball, respectively. Furthermore, steady state friction coefficient also demonstrates low but periodic variations as a function of cycle (Zoom2 on Figure 1) in the case of C90/BMG contact. The X105CrMo17/BMG friction pairs exhibits less stable, and not as periodic friction. The periodic fluctuations are not observed for all test (X105CrMo17) or the amplitude can vary from one test to another. Interestingly, tests that are demonstrating rather well-defined periodic fluctuations of friction coefficient also demonstrate the highest standard deviation of friction coefficient over each cycle of friction. The instability of friction exhibited by X105CrMo17/BMG pair might not be explained solely by the high mean friction value

(0.85). The periodicity in the fluctuations for both X105CrMo17 and C90 might result~~s~~ from periodic wear mechanisms such as the successive creation and deterioration of the interfacial layer every few hundred cycles. Such continuous modification of the interface may explain the highest variation of friction over every single cycle. Regarding, the 100Cr6/BMG friction pair, it demonstrates very stable friction coefficient.

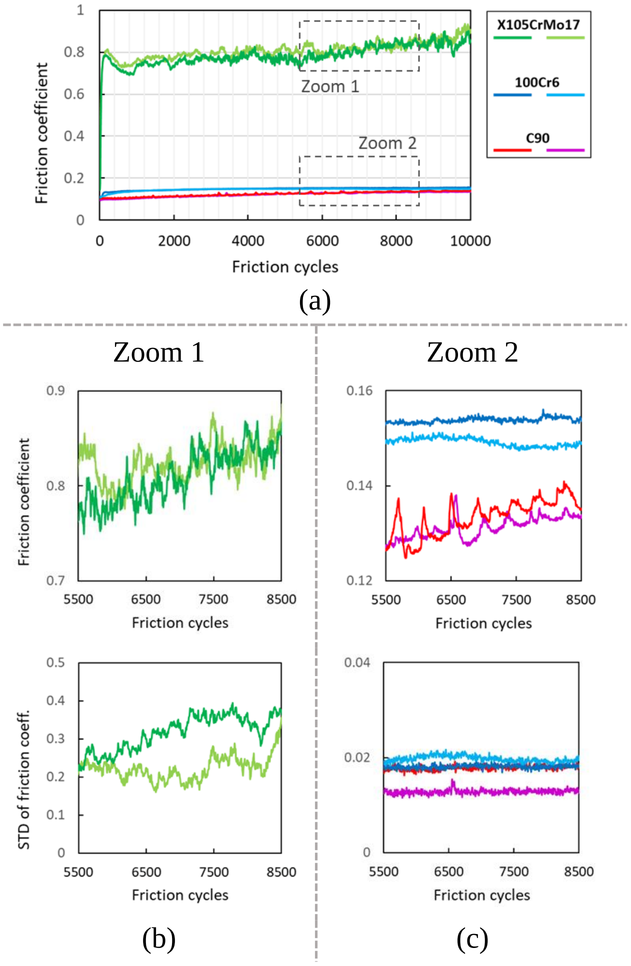

Figure 1 – (a) Friction coefficient versus friction cycles number for the 3 different friction pairs over the all test, zoomed in plots of the friction coefficients and associated standard deviation of friction coefficient over every single cycle for X105CrMo17 (b), and for both C90 and 100Cr6 (c) sliding against the $Ni_{62}Nb_{33}Zr_5$ *plate.*

Figure 2 shows the topography of the balls and the Ni-based BMG plate after friction test for the 3 contact conditions studied. In each case, both balls and plate exhibit very limited damage despite the very long sliding distance achieved.

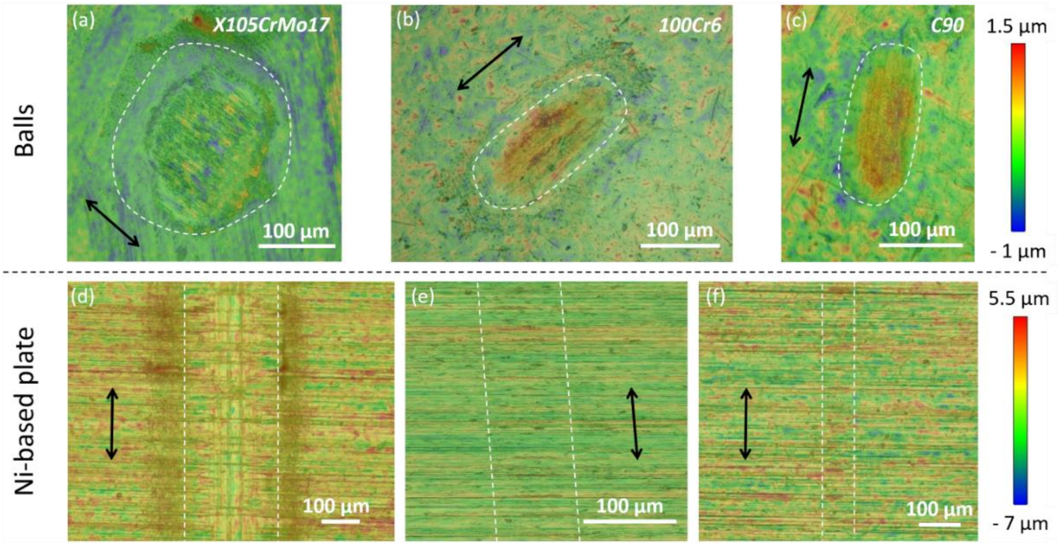

Figure 2 - Topography of the balls (top) and the BMG plate (bottom) after friction tests for the three friction pairs: X105CrMo17/BMG (a and d), 100Cr6/BMG (b and e), and C90/BMG (c and f). Optical microscopy observation (25% weighted) overlays the topography (75% weighted) of the same zone to facilitate the determination of friction scars location that are highlighted using dotted white contours. Black arrows indicate the direction of friction.

Despite very high friction coefficients measured for X105CrMo17/BMG contacts, the corresponding ball and plate surfaces showed limited wear. Friction track on the BMG plate is detectable and its width reaches 250 µm approximately. Nonetheless, calculating wear as a lost volume of material per unit of sliding distance led to values close to 1 $\mu m^3/mm$, depending on the track location considered, which is very low but consistent with previous measurements [17]. As shown in Figure 2a, the ball scar is comprised of a mixture of higher and lower asperities as compared with the mean surface height, but to a limited extent. This leads to an overall wear close to zero.

Contrary to the X105CrMo17/BMG contact, the friction scars width for the tests performed with 100Cr6 and C90 balls are only 90 µm and 80 µm, respectively. The topographic analysis of the balls demonstrates very little wear damages and very thin 3rd body layer (brown color) on top of the surface. 100Cr6 scars demonstrate two thicker patches (dark brown stripes). For both friction pairs, the friction tracks on the BMG plate are hardly detectable, there is neither detectable damages nor univocally detectable 3rd body layer or patches. The only way to find the friction track is visually thanks to dark lines of 3rd bodies that are visible at naked eyes (Figure 3). The presence of slightly more elevated asperities and lines located in the tracks can hence be associated to 3rd bodies (Figure 2e,f). That suggests the occurrence of very light material transfer and/or third-body building up. Consequently, attempts to quantify such very low wear on both balls and BMG was not successful, the limitations of the equipment being met. Wear was hence considered insignificant. Such extremely low-wear achieved when the BMG is rubbed against the 100Cr6 and C90 appears consistent with the associated very low friction coefficients measured. Although wear is more easily detectable when sliding against X105CrMo17, it remains extremely low, which is surprising for a contact demonstrating high friction (0.85).

Interestingly, although wear of the BMG can be correlated with friction coefficient, it is inversely correlated with the hardness of the counterpart. Indeed, the softest ball (X105CrMo17) induces the highest wear of the plate whereas the hardest ball (C90) induces the lowest BMG damages. This demonstrates that the tribological behaviour of $Ni_{62}Nb_{33}Zr_5$/steel contact is not directly related to the materials mechanical properties but that it is more likely driven by different tribochemical mechanisms related to the composition of the steel counterparts. The main difference being the Cr content, and the related Fe balance, further chemical investigations on the composition of the friction tracks are conducted in order to find the origin of the different tribological behaviors observed.

3.2 Friction track morphology and chemical composition

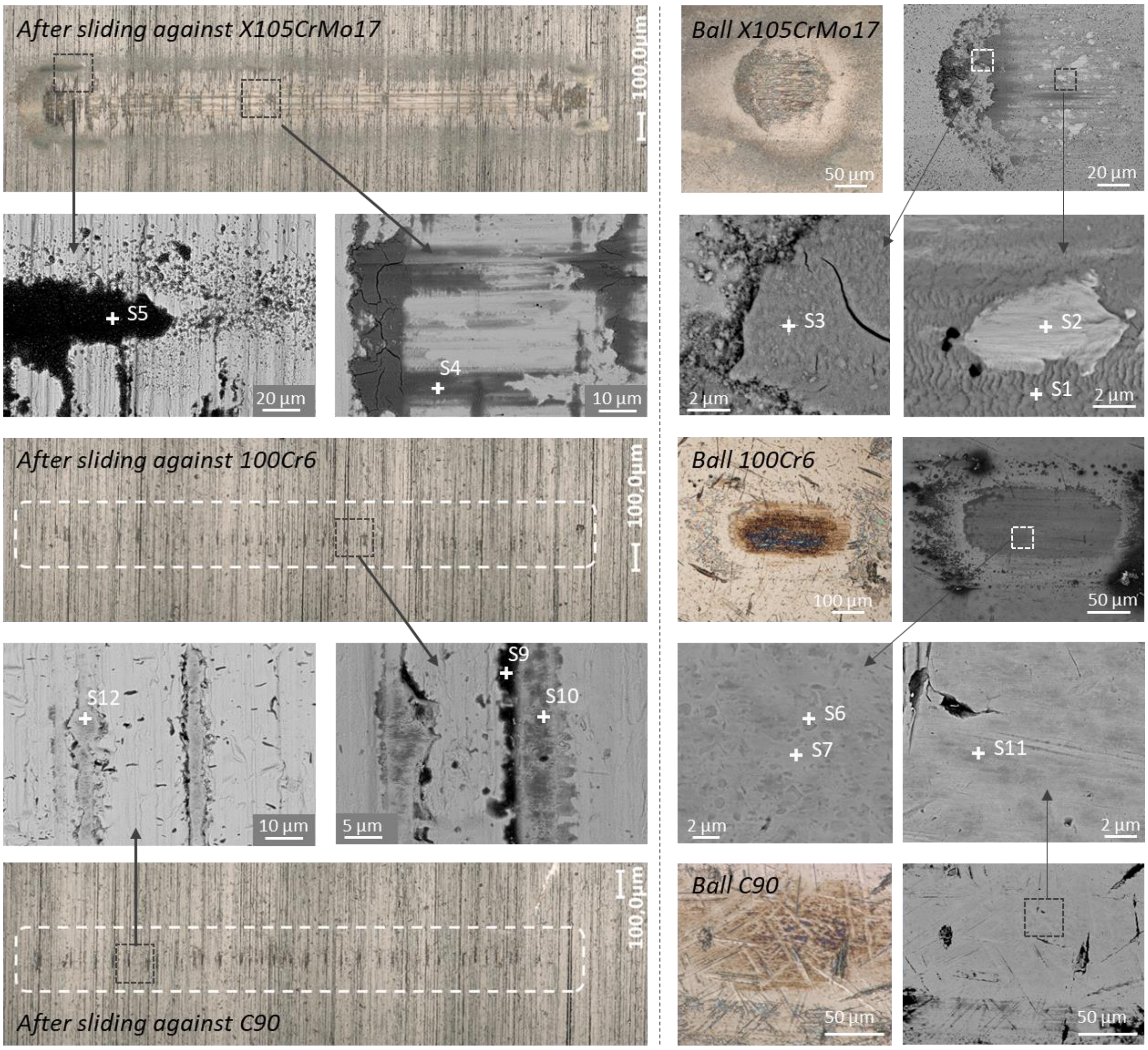

Figure 3 - Optical and SEM images of the friction track on both the BMG plate (left) and the balls (right). On the plate, friction tracks after sliding against 100Cr6 and C90 are located within the dotted white rectangular contours

Figure 3 shows the morphologies of the friction tracks observed through both optical microscopy and SEM. As discussed previously, friction tracks obtained after friction with both C90 and 100Cr6 balls are hardly detectable. The only evidence of friction is the presence of third dark bodies (identified by S9) trapped in the grooves of the surface roughness on the edge of the plastically deformed region, i.e. the upper asperities that have been transformed into a flat plateau during friction. This 3rd body contains a significant amount of O and C, low amount of Fe. Ni/Nb ratio is in line with BMG bulk composition on the top of the plateaus, a very thin layer, almost transparent light gray (identified with S12 and S10), is detectable. Those thin layers exhibit a composition rich in O, and Ni/Nb ratio of ~1 instead of 2 as in the initial BMG. Fe is also detected, but the content in the 3rd body obtained during friction with 100Cr6 (S10) is higher than after friction against C90, and it is similar to Ni and Nb content. The strongest difference between these two friction pairs is observed on the friction scars on the balls. The C90 ball demonstrates no wear, but only a very thin brown layer (optically) that is not visible under SEM. The 100Cr6 balls exhibits uniformly distributed and thicker brown 3rd body layer all over the contact ellipse. Although, blue color is observed in some places within the contact ellipse on the 100Cr6 ball, no differences between brown and blue region are observed under SEM. This can be either due to the thinness of the layers, or simply to different local optical properties. The EDX analysis (Table 2, points S6, S7, and S11) shows that Ni is detected in the region where the brown and blue layers are observed, which means that Ni has been transferred from the BMG to the ball. Oxygen is also detected, which demonstrates the presence of oxides that, however, cannot be identified through EDX. The 100Cr6 ball also exhibits particles ejection outside the contact ellipse, in the sliding direction. Interestingly, ejected particles have a similar morphology than the those ejected outside the friction tracks on the plate (identified by S5) during friction of X105CrMo17 ball on the BMG. Particles appear loose and < 1µm in size, they are packed on the edge of the friction tracks. They are mostly comprised of Ni, Nb, O, and Fe. Interestingly Ni and Nb content are similar, which differs from the BMG where the atomic percentage of Ni is twice the Nb. The significant level of O demonstrates oxidation.

Different 3rd bodies resulting from friction between X105CrMo17 ball on the BMG are observed inside the friction tracks. First, heavily compacted 3rd body, which still exhibits granular texture, is observed (identified by S3 for the ball, and S4 for the plate). In addition, on the ball, a thick 3rd body distributed in patches (identified by S2) and sitting in top of "fish scale like" 3rd body (identified by S1) is detected. EDX analysis shows very high concentration of Ni in the composition of these 3rd bodies, as compared to Nb, particularly in the white 3rd body (S2). Fe and Cr are also detected, with Fe/Cr ratios of ~4.4 (S1) and 4.6 (S2), which does not differ significantly from the bulk X105CrMo17. The white 3rd body patches are large and thick, they appear to carry most of the load inside the contact. Ejected particles are showing composition that is rich in Nb as compared to the initial composition of the BMG. Nb and Ni oxides are known to be softer than Cr oxide [17,21] and would thus be expected inside the friction track to minimise the energy dissipated by friction. Finally, for all spectrum (S1 to S12) Nb/Zr ratio remains constant (~6), which is similar to the original BMG composition. Zr hence appears to play a minor role in the friction accommodation mechanisms.

Table 2 - EDX analysis of the regions (S1 to S12) identified in Figure 5. EDX analyses are conducted at 10 kV. C content is given considering it is heavily detected in some cases, however discussion is limited due to the high probability of C pollution during SEM imaging.

Counterpart	Sample	Spectrum	Elemental composition (atomic %)						
			Ni	Nb	Zr	Fe	Cr	O	C
X105CrMo17	Ball	S1	**16.9**	5.7	1.0	**15.1**	**3.4**	**48.0**	10.0
		S2	**69.4**	1.5	0	**6.5**	**1.4**	6.8	14.5
		S3	**13.0**	**12.6**	2.1	3.0	0.7	**63.0**	6.7
	Plate	S4	**18.2**	**12.6**	2.2	**4.8**	1.0	**54.4**	6.9
		S5	**12.2**	**17.7**	3.1	**4.3**	1.1	**51.6**	10.0
100Cr6	Ball	S6	**4.4**	0.8	0.1	62.0	4.5	**8.0**	**19.8**
		S7	**3.3**	0.7	0.1	76.8	0.8	**5.12**	**12.3**
	Plate	S9	**6.1**	**3.7**	0.1	2.3	0.1	**16.4**	**70.5**
		S10	**11.4**	**11.0**	2.0	**11.5**	0.5	**58.2**	4.3
C90	Ball	S11	**6.6**	1.3	0.2	**63.8**	0.2	**16.3**	11.0
	Plate	S12	**24.3**	**20.9**	3.7	3.6	0	**39.1**	8.4

Overall, the EDX analysis essentially tells that Ni is preferentially transferred to the counterface as compared to Nb, and both are mixed with Fe, and O. Oxidation hence happens to be accentuated by friction. Combined with SEM images and topographic analysis, this strongly suggests a soft adhesive wear mechanism implicating some material transfers from the plate to the ball. It also shows that the plastically deformed BMG material sees its composition changing from a Ni/Nb ratio of ~2 to Ni/Nb ratio of ~1. The high friction of X105CrMo17/BMG and low friction of 100Cr6/BMG pair (where Ni, Nb, Fe exhibit similar concentration (S10)), imply complex tribochemical processes. EDX does not allow to study the impact of Cr, because the content is either too low in the 3rd bodies, or the 3rd body layers are too thin. Consequently, complementary vibrational and top surface chemical analysis are performed using NanoSIMS, XPS and Raman.

XPS analysis (Figure 4) demonstrates that the surface of the $Ni_{62}Nb_{33}Zr_5$ BMG is essentially comprised of Nb_2O_5 oxide, and of ZrO_2 oxides to a lower extend. Ni is more detected in its metallic form. That is consistent with previous studies where the native oxide of the $Ni_{62}Nb_{38}$ is shown to be Nb_2O_5 [22,23]. Although the spot size in XPS analysis was wider than the largest friction track (from X105CrMo17 friction test), the results obtained in the case of X105CrMo17 emphasize the stronger impact of friction on Ni based material, as shown by EDX. Ni is more detected as oxide and hydroxides than as metal, while the low contribution of NbO_2 related peaks in the Nb related peaks is disappearing. Zr is not affected at all. XPS analysis did not show any signal from Fe and Cr (Figure S8 in Suppl. Material). After friction with C90 and 100Cr6, XPS does not demonstrate any changes, which further emphasized the very local friction induced damages of the surfaces.

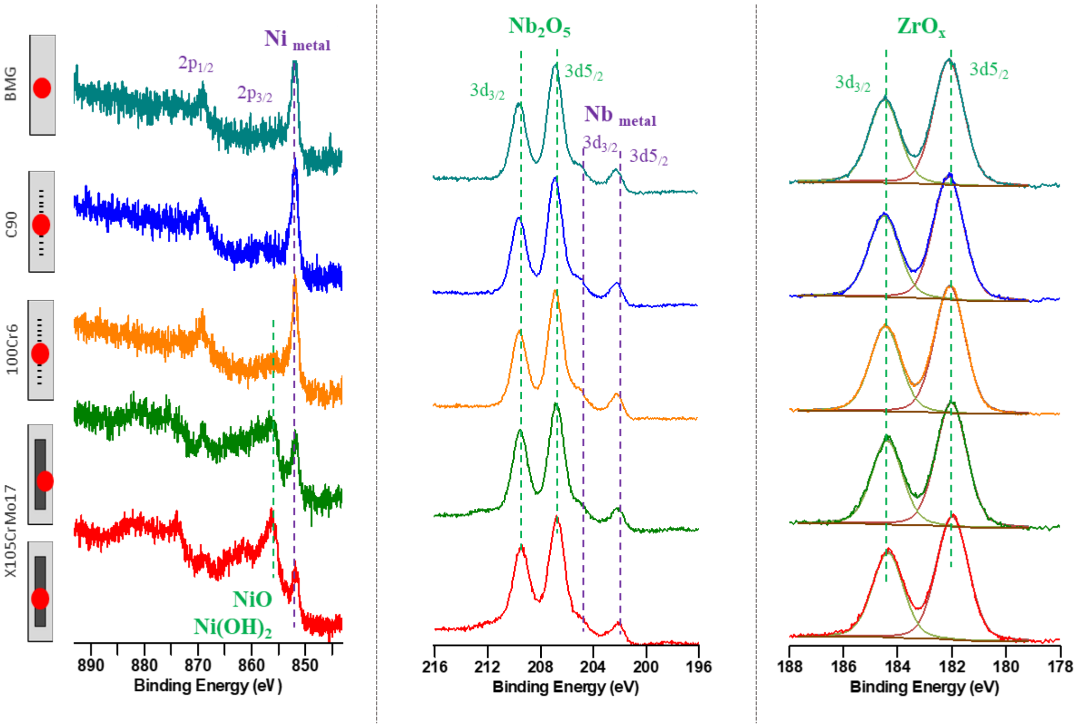

Figure 4 – Ni2p, Nb3d, and Zr3d related pic from XPS analysis of the friction track of the BMG plate as a function of the sliding counter material

In order to look into local composition of the friction track and the 3rd body materials created during friction, NanoSIMS analysis have been conducted. Mapping of chemical element comprising the BMG and the 3rd bodies, as well as spectra (in both positive and negative ion detection modes) are presented. Figure 5 and Figure 6 are presenting the results from X105CrMo17/BMG friction tests, and also the results from the pristine BMG material on the edge of the friction track. Results from C90/BMG and 100Cr6/BMG can be found in SI (Figure S4 to S7). Chemical mapping (Figure 5 and Figure S8) confirm that Ni is heavily detected in the 3rd bodies, along with Fe and Cr (for both 100Cr6 and X105CrMo17 contacts). In the regions where Fe and Cr are the most detected, Nb and Zr are the less detected.

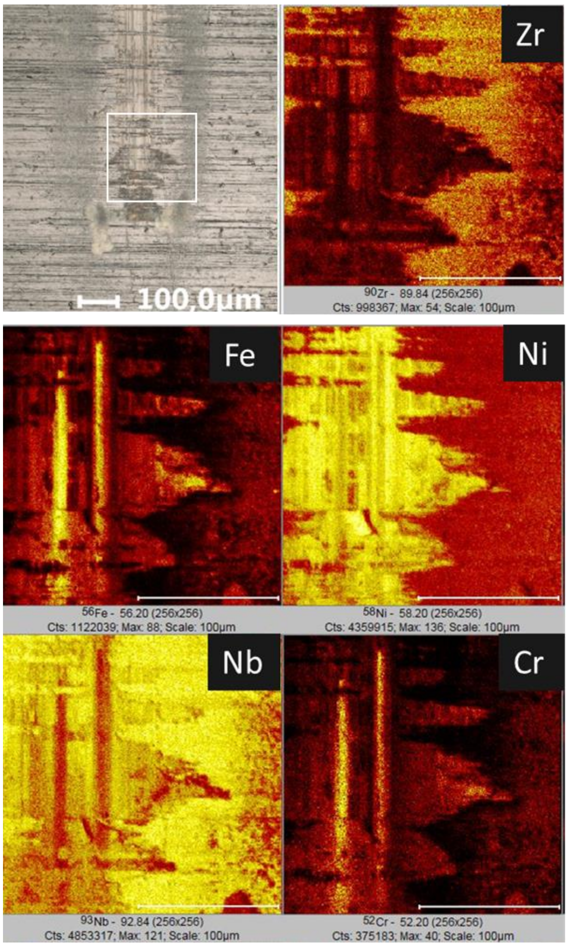

Figure 5 - Mapping of the distribution of the main metal element after sliding between the BMG and the X105CrMo17 stainless steel ball.

The mass spectra of the pristine BMG (Figure 6) demonstrates that Nb and Zr are the most detected in the pristine region of the BMG, which confirms previous observations regarding the composition of the NiNb based BMG surface composition [23]. Ni is detected, mostly as Ni^+. Its intensity of detection (highest pic around 5e-7 counts), is intermediate between the detection Zr^+ (main pic at 3e-7 counts) and Nb^+ (6e-7 counts). Contrary to Nb and Zr, Ni is not demonstrating any detection of oxides. Nb oxides are the most detected, in both positive and negative detection modes. The magnitude of NbO_3^- detection is 5.5x larger than NbO_2^-. That ratio differs from pure Nb_2O_5 reference spectrum which exhibits a factor of ~7.5 between the magnitude of detection of these two ions [24]. However, NbO_3^- detection is 17x larger than $Nb_2O_5^-$ (Figure S7), which is ~~getting~~ different from pure amorphous Nb_2O_5 for which the ratio is ~13x [24]. $C_xH_yO_zNbZr^+$ compounds are highly detected in positive detection mode, as compared to $Nb_2O_3^+$ and $Nb_2O_4^+$ (Figure S7). Consequently, the surface of the pristine BMG most likely contains both Nb_2O_5, NbO_2 oxides, and some $C_xH_yO_zNbZr$ compounds. Such overall observations are consistent with XPS analyses where Ni is mostly detected in its metal form, and both Nb and Zr as oxides (Figure 4).

The composition of the 3rd bodies obtained during friction is exhibiting significantly different compositions between X105CrMo17, and the other two contacts (C90 and 106Cr6) which are exhibiting similar trends (Figure 6 and Figures S4 to S9).

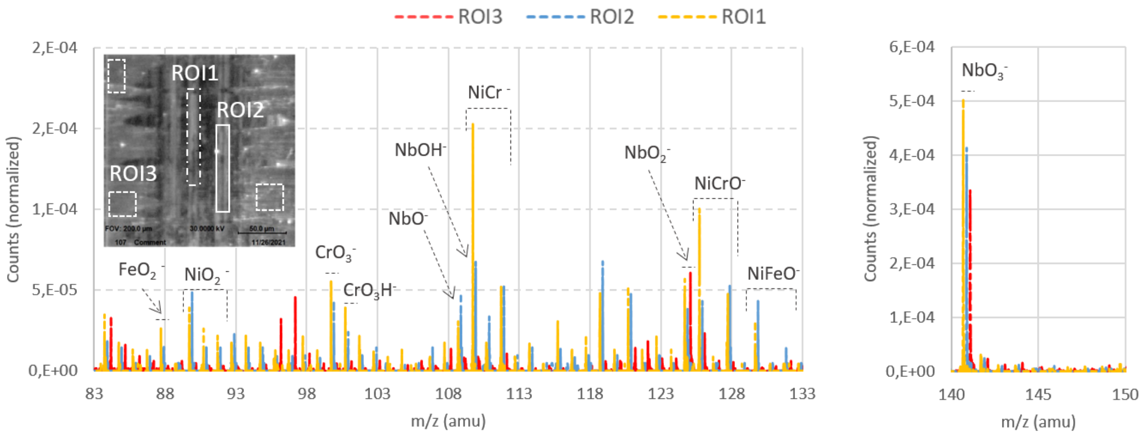

(a) Negative detection mode

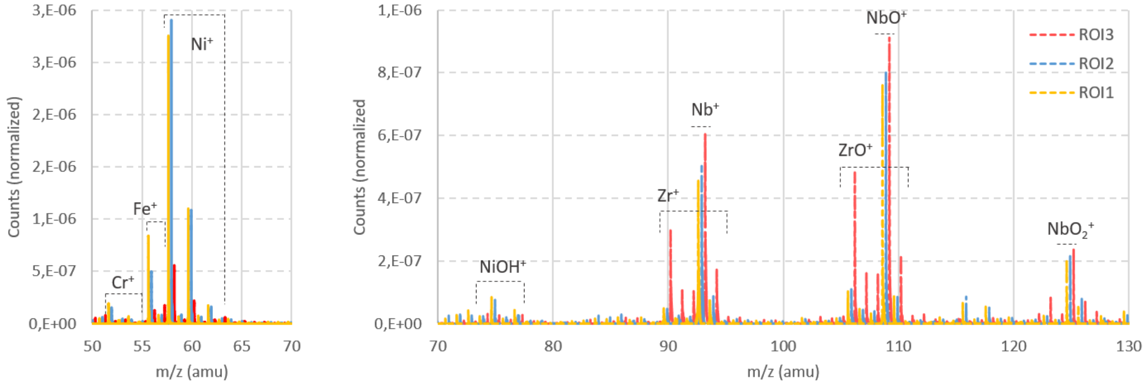

(b) Positive detection mode

Figure 6 - NanoSIMS mass spectra in both negative (a) and positive (b) detections modes, obtained from friction test with X105CrMo17 sliding against BMG. ROI3 corresponds to pristine surface outside the friction track. ROI1 and ROI2 are two regions of interests chosen on 3rd body materials presenting high and low level of Cr on chemical maps, respectively. ROI3 related spectra results from averaging spectra over 3 different locations.

In the cases of C90/BMG and 100Cr6/BMG contacts, the Ni content versus Zr and Nb do not change significantly from the pristine BMG material (Figures S5 and S7). It indeed lies within the same range for C90/BMG contact, and it decreases slightly for 100Cr6/BMG contact (Figures S4 and S5). In both cases, NiOH$^+$ ions are detected at a low content. The detection of Nb oxide related ions is significant (Figures S4 and S6). The ratios of intensity between them however differ from the pristine material (Figure 6). NbO$_3^-$ peak exhibits intensity of detection 7x to 8x larger than NbO$_2^-$, which is typical of amorphous Nb$_2$O$_5$ [24]. Ratios of NbO$_3^-$ and Nb$_2$O$_5^-$ is however around 35 and not 13 as in amorphous Nb$_2$O$_5$, that implies a higher abundance of dimeric and trimeric Nb oxide ions. It has to be noted that 3rd bodies from both contacts are demonstrating the significant presence of Fe$^+$, particularly in the 100Cr6/BMG case. In the latter case, Cr$^+$ is detected only in the thicker material, and as Cr$^+$ fragments. That means Cr is either remaining in its metallic form or its oxide form is not significantly present. ToF-SIMS spectra also shows that FeNb-oxyde is highly detected (Figures S5 and S7) in both contacts. The 100Cr6/BMG contact however sees the net increase in detection of NiNb-oxides, and of both ZrFe- and ZrNi oxide compounds (Figure S7). FeNb-oxyde however remains the most detected. The formation of bi-metal oxides, and the additional combination of Nb to Zr in the form of C$_x$H$_y$O$_z$NbZr$^-$ and NbZr hydroxides, may both explain the difference observed with amorphous Nb$_2$O$_5$ ToF-SIMS data from literature. A change in the crystallinity of the material, induced by friction, may also impact the bulk fragmentation under the ion bombardment. Moreover, a change in the surrounding chemical state can impact the ionization of the different elements (matrix effect) [25]. Overall, friction induces the formation of Nb_xO_y oxide, and one main bimetal oxide (FeNb-oxide) in C90/BMG case. In 100Cr6/BMG case, it induces the formation of Nb_xO_y oxide, 4 bi-metal oxides ($FeNbO_x$ – the main one-, $NiNbO_x$, $ZrFeO_x$, and $ZrNiO_x$), and of Ni-oxide to a very low extend.

In X105CrMo17/BMG case, Ni is significantly more detected than Nb and Zr in the 3rd body. Ni^+ intensity of detection is 6x higher than Nb^+, while Zr related ion detection is significantly reduced (Figure 6b). Fe^+ is detected with a maximum amplitude similar to $NibO^+$, which is similar to what is observed with both C90 and 106Cr6 contacts (Figures S5 and S7). Cr^+ detection demonstrates higher detection than Zr related ions, and it is equivalent to NbO_2^+ ions. $NiOH^+$ is also detected but to a lower extend than NbO_2^+, which differs from both C90 and 106Cr6 contacts (Figures S4 and S5). Such a high contribution of Cr to the spectra is confirmed by the negative ion detection (Figure 6a) where CrO_3^-, CrO_3H^-, $NiCr^-$, and $NiCrO^-$ are clearly detected. Cr(VI) oxide amplitudes of detection is similar to those of NbO^-, $NbOH^-$, NbO_2^-, and NiO_2^-. Surprisingly, insignificant detection of CrO_2 related ions is observed. $NiFeO^-$ detection is higher, in amplitudes, than FeO^- detection, but it is similar to NiO_2^-, NbO^-, $NbOH^-$, and NbO_2^-. The NbO_3^-/ NbO_2^- detection ratio is around 10, $NbO_3^-/Nb_2O_5^-$ detection ratio is around 13 and 16 for ROI1 and ROI2 respectively, which is close to pure amorphous Nb_2O_5 [24]. At high mass number (Figure S9), bimetal oxides are detected. Contrary to what is observed with 100Cr6 and C90 contacts, they mostly contain Cr and not Fe. CrNb-oxides are the most detected, and then comes NiNb-oxides and what appears to be ZrCr-oxides. Overall, NiCr-oxides appears the most intensely detected, followed by Nb-oxides, and Cr-M-oxides (M=Nb, Zr). Then comes Cr- and Ni- oxides. Finally, $C_xH_yO_zNbZr$ compounds are barely detected (Figure S9), as compared to 100Cr6 and C90 (Figures S4 and S5) and as compared to pristine material (Figure 6 and S7). Compared to 100Cr6 and C90 related data, Nb oxide is significantly less present in the 3rd body to the benefit of Cr-M-oxides (M=Ni, Nb, and Fe to a lower extend), Cr-oxides, and Ni-oxides. However, Nb oxide appears to getting closer to Nb_2O_5. The preferential creation of Cr(VI) oxide, rather than Cr(IV) oxide remains unclear.

Given the difficulty of identifying the nature of the compounds making up the third body, micro-Raman spectroscopic analyses were carried out on the friction tracks (Figure 7). Low laser power, less than 5 mW, was used to avoid the damage of the 3rd bodies.

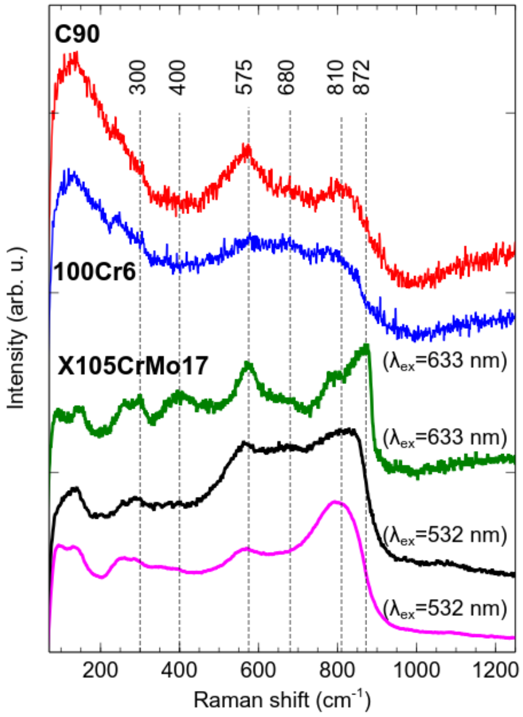

Figure 7 - Raman spectra measured in the friction tracks on the BMG plates after friction against C90, 100Cr6, and X105CrMo17 steel balls. Laser wavelength is indicated in brackets in the figure legend.

In the case of C90 and 100Cr6 steels, the intensity of the Raman bands was very low, and the presence of a high background signal made their detection difficult. The Raman spectra show in both cases unresolved contributions below 350 cm^{-1} and broad overlapping bands in the 500-900 cm^{-1} range, with main components around 575, 680 and 810 cm^{-1}. First, these spectra do not match the Raman fingerprint of tetragonal or monoclinic ZrO_2 [26], nor that of NiO [27]. In contrast, the band at around 680 cm^{-1} corresponds to the position of the main band in the Raman spectrum of Nb_2O_5, which also features smaller bands at around 315 and 227 cm^{-1} [28,29]. This spectrum is modified in the case of Ni-Nb mixed oxides, which exhibit a main band around 650 cm^{-1} and a higher frequency band around 840 cm^{-1} [30]. EDX analysis of the debris showed the presence of Nb, and XPS analysis revealed the oxidized Nb(V) state. All these results support the formation of niobium oxide, and possibly Ni-Nb and/or Fe-Nb mixed oxides. Concerning iron oxides, only the component at around 680 cm^{-1} (Figure 7) is in the range where magnetite, Fe_3O_4, and maghemite, γ-Fe_2O_3, display their highest frequency and most intense Raman bands [31]. The component observed here at around 810 cm^{-1} cannot be attributed to $NiFe_2O_4$ either, whose highest frequency band is at around 700 cm^{-1} [27]. By contrast, the Raman spectra of different metal niobates show Raman bands up to 800-900 cm^{-1}.

Husson et al. [32] reported an extensive study of the Raman spectra of niobate compounds MNb_2O_6 with M=Ca, Cd, Co, Cu, Fe, Mg, Ni and Zn. All show similar Raman spectra above 380 cm^{-1} including an intense and sharp peak in the 840-910 cm^{-1} range associated with Nb-O stretching for terminal oxygen atoms that link NbO_6 octahedra to adjacent MO_6 ones. De Luna et al. [33] confirmed this result for $NiNb_2O_6$, which shows an intense and narrow peak at 883 cm^{-1}. In our case, the Raman spectra of the 3rd bodies for C90 and 100Cr6 counterparts do not show such a sharp peak, and the highest frequency bands appear at lower frequencies (~810 cm^{-1}). Like the bivalent metal niobates, the Raman spectra of the trivalent metal niobates also show high-frequency vibrations due to the stretching modes of the NbO_6 octahedra, but not the intense, narrow peak observed for MNb_2O_6 compounds in the 840-910 cm^{-1} range. In particular, the spectrum of monoclinic $FeNbO_4$ [34–37] show bands at 820, 601, 470, 397 and 279 cm^{-1} due to the different Nb-O stretching modes. The main characteristics of this spectrum correspond to those of the spectra obtained in the present work (Figure 7) for C90 and 100Cr6 steels. The apparent detection of Ni-niobates and Fe-niobates are consistent with ToF-SIMS analyses which demonstrate the detection of related fragments (Figures S5 and S7).

For the X105CrMo17/BMG case, the Raman spectra obtained in different points (Figure 7) display a flat background below 500 cm^{-1} which allows to observe bands at about 260-300 and 400 cm^{-1}. Above 500 cm^{-1}, stronger bands are again observed, centered around 575 and 810 cm^{-1}, and sometimes extending to near 870 cm^{-1}, which may indicate the local formation of nickel niobate, $NiNb_2O_6$ [33]. We can recall that XPS analysis of the debris clearly showed nickel oxidation in the case of X105CrMo17/BMG, unlike for C90/BMG and 100Cr6/BMG. Together with Ni and Nb, EDX analysis detected iron, as well as zirconium and chromium in lower concentration. Consequently, it is possible for various mixed niobium oxides and/or metal niobates to coexist in the friction tracks, including $CrNbO_4$ [38]. The latter is also clearly detected in ToF-SIMS spectra (Figure S9). $NiNb_2O_6$ fragments are not detected as much in the ToF-SIMS spectra. Contribution from common Nb_2O_5 oxides [39–41], even after being amorphized mechanically [40] appears very low, which further suggest coexistence of mixed niobium oxides and/or metal niobates.

Regarding the surprising detection of Cr(VI) oxides in ToF-SIMS spectra of the X105CrMo17/BMG case, Raman spectroscopy allows to dissociate Cr(VI)-oxides from Cr(IV)-oxides [42,43]. Using laser wavelength of 647.1 nm, Maslar & coworkers [43] reported that the Cr^{VI}-O bending mode lies in the 316-405 cm^{-1} shift range, and the Cr^{VI}-O stretching mode in the 840-1003 cm^{-1} shift range. Symmetric and asymmetric stretching modes of Cr^{VI}-O-Cr^{VI} bridging, and its bending modes have been discussed as well. The range of Raman shift corresponding to the stretching mode of O-Cr^{VI}-O is also addressed. They all lie in the 218-338 cm^{-1}, 719-790 cm^{-1} or 719-848 cm^{-1}, and 818-848 cm^{-1} shift ranges. The rocking mode of Cr^{VI}-O-Cr^{VI} bridging unit has also been reported in 230-379 cm^{-1} range, and external vibration modes around 211 cm^{-1} and in lower Raman shifts. All those ranges cover the observed broad/shoulder pics of X105CrMo17 at 633nm laser wavelength (Figure 7). Raman shift in the range of 700-900 cm^{-1} has also been observed for Cr(VI) compounds in other study [44]. From Kim et [27] and Maslar et [45], it can be concluded that NiO, $NiFe_2O_4$, and $NiCr_2O_4$ are not contributing to the Raman sprectra in the present study. However, α-CrOOH (from Cr(III)) might slightly contribute to the Raman spectra in the range of 540-630 cm^{-1} [45]. That may imply a very small but possible contribution of Cr_2O_3 compounds. Detection of $Nb(HC_2O_4)_5$ compounds might be questioned, although one of the main pic around 930 cm^{-1} is not detected [41]. ToF-SIMS study indeed showed the presence of $C_xH_yO_zNbZr$ compounds.

Consequently, considering the band shifts of $NiNb_2O_6$ [33], $CrNbO_4$ [38] agree well with the band shifts observed in the Raman spectrum (Figure 7). Furthermore, considering that few band shits from Cr(VI) oxides are not strongly detected, it can be assumed that metal niobates are the most detected. However, Cr(VI)-oxides cannot be completely excluded, and the question regarding its origin remains open.

Figure 8 summarizes the main results from the study. Different friction coefficient and wear behavior have been observed, although the contact configuration is similar between all test except from the Cr content of the sliding steel ball. First, the friction coefficient increases as the Cr content increases inside the steel ball. Such observation confirms the hypothesis drawn in a previous study regarding the effect of Cr on the friction behavior of $Ni_{62}Nb_{33}Zr_5$ BMG [17]. In that same study, 100Cr6 steel ball was used and friction coefficient varied from 0.1 to 0.9 when the initial maximum Hertz contact pressure was 310 MPa and 680 MPa, respectively. In the present study, the friction coefficient obtained is 0.15 with 420 MPa initial maximum Hertz contact pressure. That also support the hypothesis that the friction can be load dependent, as increasing load may help triggering the tribochemical processes involved. Using three different counterparts with different Cr content, the present study sheds light on the role of Cr in the creation of 3rd body materials responsible for high friction. In the case of C90 steel, which does not contain Cr, the 3rd body is only comprised of Nb, Ni, and Fe based oxides. Nb_2O_5 remains the most present, even though it is to a lower extend than in the pristine surface. FeNb-oxide was shown to be created under friction, and its intensity of detection demonstrates that its presence is significant. Common iron oxide, which plays a major role in friction of CuZr based BMG against steel [16–18] in similar contact conditions, and which led to high coefficient, is detected to a limited extend. Finally, some Ni oxide is created under friction, but its detection is rather low as compared to the other monovalent and divalent metal oxides. Yu et al [46] demonstrated that when $CoCrO_4$, $NiCr_2O_4$, $FeNbO_4$, $NiNb_2O_6$ inorganic acid salts are created during full oxidation of $CoCrFeNiNb_x$ high entropy alloy, it results in the formation of a thin, dense, and compact tribolayer with good wear resistance, although providing relatively high friction (0.5 to 0.7). That hence further supports the results of the present study. $FeNbO_4$, and $NiNb_2O_6$ related oxides are indeed highly detected alongside Nb_2O_5. The latter is undertaking lubrication while the other must likely help in protecting the surface from damages.

When Cr comes at play, in the composition of the ball, friction rises and 3rd body materials starts to build up on both plate and ball surfaces. It remains however very thin, and it maintains very high anti-wear properties. The loss in lubricious properties increases with the Cr content in the steel. Compared to the C90/BMG case, the 3rd body created in the 100Cr6/BMG contact contains some Cr in its composition. It appears to remain mostly in its metallic form as no oxides are significantly detected. There is nonetheless a slight change in the detection of Nb_2O_5 related fragments, i.e. a change in the oxide itself. Besides Nb_2O_5 oxide, FeNb oxide remains significantly present in the composition of the 3rd body, and NiNb-oxides are slightly more detected. The small increase in friction when passing from C90 to 100Cr6 might be related to the change in the Nb_2O_5 oxide, in combination with $FeNbO_4$, and $NiNb_2O_6$ related material that are slightly more detected.

When the Cr oxide becomes significant, as in the X105CrMo17 case, Cr containing material takes over and becomes the main constituting element of the 3rd bodies. Ejected material is essentially comprised of Nb_2O_5 (in proportion similar to the pristine surface), and Ni-oxides similar to those comprising the 3rd body in both C90/BMG and 100Cr6/BMG contacts. Ejected third bodies also contains some NiCrO, NiFeO, and Cr(VI) oxides (presumably CrO_3). FeNb-oxide are almost not detected, but they are replaced by CrNb-oxides. Those divalent metal oxides, particularly those containing Cr, are believed to be the one that are essentially comprising the 3rd body remaining inside the X105CrMo17/BMG contact. It is also assumed that they are leading to high friction, while maintaining very low wear (wear volume hardly measured). The 3rd body inside the friction track, and consequently the 3rd body taking part in the accommodation of friction, exhibits two different morphologies. One is granular, and one is a thick highly compacted that is carrying most of the load. The latter sits on top of a layer exhibiting a "fish-scale" morphology, which could be associated to adhesive contact to some extend. The literature shows that hexavalent Cr coating exhibits high friction (0.6) when sliding against X105CrMo17 steel at 620 MPa maximum Hertz contact pressure, 116 mm/s [47]. Under rather high contact pressure (1 GPa) but similar sliding speed (8 mm/s) Ni-Fe-Cr alloy exhibits high friction (0.7) when sliding against hardened bearing steel ball [48]. Finally, 3rd bodies containing Cr_2O_3 and $CrNbO_4$ oxides have been reported to be associated to high friction (0.55 to 0.9) and low wear rate [49], as well as $NiCr_2O_4$, $FeNbO_4$, $NiNb_2O_6$ [46]. That hence makes the results of the present study consistent with results obtained with bulk materials in the literature.

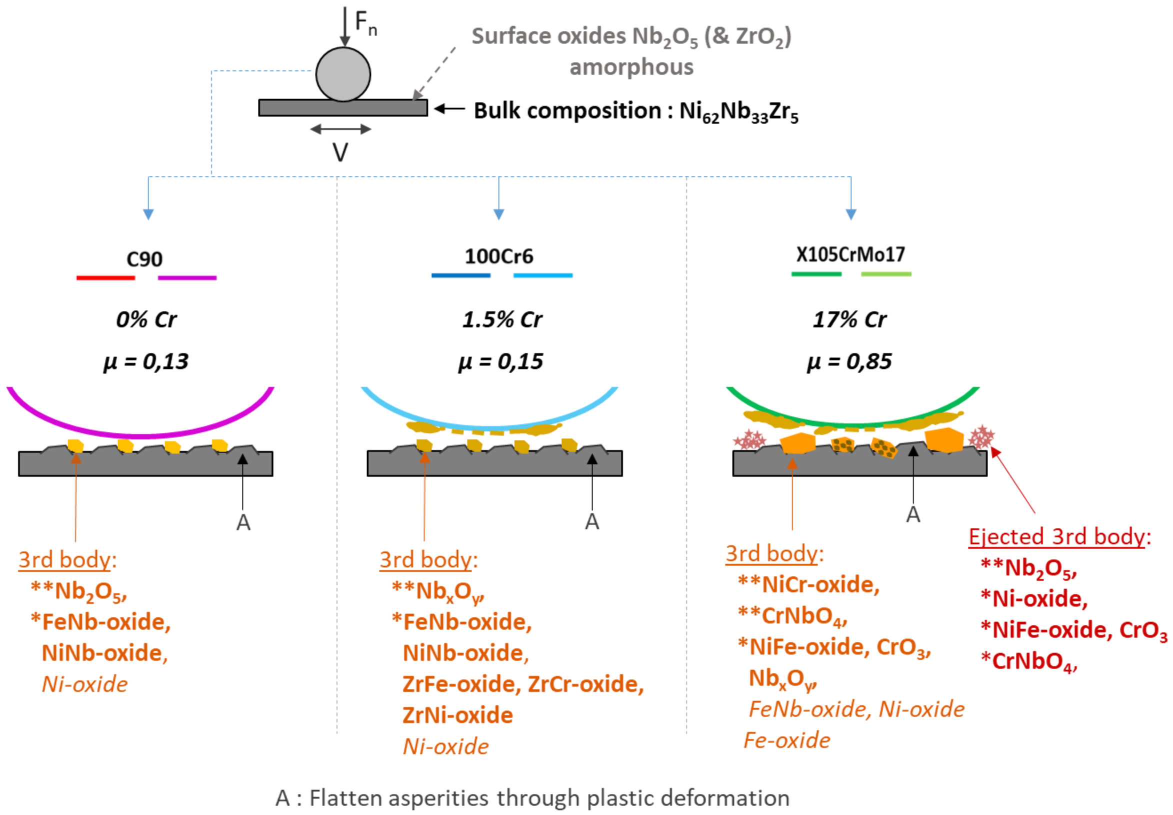

*Figure 8 – Schematic summarizing the main conclusion of the study regarding (i) the 3rd body composition within the interface and the ejected one (in the case of X105CrMo17), and (ii) wear; both in relation to the Cr content of the counter body and the value of the steady state friction coefficient. Number of * indicate the predominant compounds. Compounds in plain font are believed to be detected as traces.*

4 Conclusion

In this work, the tribological (friction and wear) behavior of $Ni_{62}Nb_{33}Zr_5$ bulk metallic glass (BMG) in friction against three different steels has been investigating. The purpose of the study was to investigate if the friction response of $Ni_{62}Nb_{33}Zr_5$ could be driven through the Cr content in the sliding counterpart, as suggested in a previous study. The chosen steels were C90, 100Cr6 and X105CrMo17 because they are exhibiting different content of Cr (0%, 1.5%, and 17% respectively), and similar content of C. Moreover, they are all exhibiting similar mechanical properties.

Overall the study sheds light on the tribochemistry dependence of $Ni_{62}Nb_{33}Zr_5$ bulk metallic glass on the Cr content of steel counterparts. Under exactly the same contact conditions, the study showed that the steady state friction coefficient increased from 0.13 to 0.15, and then to 0.85 with the increase of Cr content from 0%, to 1.5% to 17%. Wear remained low enough to not be measurable. However, the 3rd body material was more present inside the friction tracks when friction was high, i.e. that C90/ $Ni_{62}Nb_{33}Zr_5$ contact exhibit very low amount of 3rd body material while X105CrMo17/ $Ni_{62}Nb_{33}Zr_5$ contact exhibit 3rd body materials on both samples with thick patches locally. EDX, ToF-SIMS, and Raman Spectroscopy allowed to show that the high friction is explained not by the quantity of third bodies, but rather by its nature. The lowest friction is found to be related to Nb_2O_5 oxide (predominant) and $FeNbO_4$, and then NiNb-oxide. Nb_2O_5 oxide, a ductile material, most likely undertake lubrication while $FeNbO_4$ and NiNb-oxide help protecting the surface from further severe wear. The 100Cr6/

$Ni_{62}Nb_{33}Zr_5$ contacts exhibits a slightly higher friction than the C90/ $Ni_{62}Nb_{33}Zr_5$ contact due to a change in Nb_2O_5 compounds, and due to slightly higher content of $FeNbO_4$ and NiNb-oxide that are shown to provide high friction but low wear. Moreover, ZrM-oxide (M=Fe, Cr, Ni) are detected and must play a role in that increase in friction coefficient.

The X105CrMo17/$Ni_{62}Nb_{33}Zr_5$ contact, which resulted in 0.85 friction coefficient, demonstrates that the third body inside the friction track is rich in NiCrO, $CrNbO_4$, NiFe-oxide, and Cr(VI)-oxide. The ejected third body is rich in Nb- and Ni-oxides, and less in $CrNbO_4$, NiFe-oxide. NiCrO, $CrNbO_4$, NiFe-oxide, and Cr(VI)-oxide have been showed to exhibit high friction in the literature, which is hence in line with the present results. Although metal niobates are the most likely created oxides under friction, detection of Cr(VI)-oxyde by ToF-SIMS remains an open question. Further investigations are needed to clarify its existence, and to quantity the amount produced as compared to the total wear volume of wear material. One might take it into account when considering the use of $Ni_{62}Nb_{33}Zr_5$ against Cr containing material.

Finally, the study shows that under dry contact condition and moderate contact pressure, long lasting low friction (< 0.15), and low wear are accessible in steel/$Ni_{62}Nb_{33}Zr_5$ contact, which further supports the use of metallic glasses in tribological application.

5 Acknowledgement

The authors wish to sincerely thank Hugo Lallement (master internship student) for his contribution to friction tests campaign. This work was supported by TriboRAMA project (contract ANR-19-CE08-0015), TeC-Lub project funded by Conseil Régional de Bourgogne-Franche-Comté (contracts RECH-N2FON-000070 and RECH-N1INV-000037), internal funding from Vulkam Inc. This work was also partially supported by the EIPHI Graduate School (contract ANR-17-EURE-0002).

6 References

[1] W. Klement, R.H. Willens, P. Duwez, Non-crystalline Structure in Solidified Gold–Silicon Alloys, Nature. 187 (1960) 869–870. https://doi.org/https://doi.org/10.1038/187869b0.

[2] D.C. Hofmann, R. Polit-casillas, S.N. Roberts, J. Borgonia, R.P. Dillon, E. Hilgemann, J. Kolodziejska, L. Montemayor, J. Suh, A. Hoff, K. Carpenter, A. Parness, W.L. Johnson, A. Kennett, B. Wilcox, Castable Bulk Metallic Glass Strain Wave Gears : Towards Decreasing the Cost of High-Performance Robotics, Sci. Rep. (2016) 1–11. https://doi.org/10.1038/srep37773.

[3] M. Ishida, H. Takeda, N. Nishiyama, K. Kita, Y. Shimizu, Y. Saotome, A. Inoue, Wear resistivity of super-precision microgear made of Ni-based metallic glass, Mater. Sci. Eng. A. 449–451 (2007) 149–154. https://doi.org/10.1016/j.msea.2006.02.300.

[4] M. Ishida, H. Takeda, D. Watanabe, K. Amiya, N. Nishiyama, K. Kita, Y. Saotome, A. Inoue, Fillability and Imprintability of High-strength Ni-based Bulk Metallic Glass Prepared by the Precision Die-casting Technique, Mater. Today. 45 (2004) 1239–1244.

[5] A. Merstallinger, L. Baca, N. Stelzer, Z. Kovacova, E. Neubauer, A. Toufine, A. Makaya, Cold Welding and Friction in Vacuum Of BULK METALLIC GLASS (BMG) MADE BY POWDER BASED PROCESSES FOR USE IN SPACE, in: Proc. 20th Eur. Sp. Mech. Tribol. Symp. - ESMATS 2023, 2023.

[6] K. Matsubara, M. Danno, M. Inoue, Y. Honda, N. Yoshida, T. Abe, Characterization of titanium particles treated with N2 plasma using a barrel-plasma-treatment system, Phys. Chem. Chem. Phys. 15 (2013) 5097–5107. https://doi.org/10.1039/c3cp44434a.

[7] R. Slatter, R. Degen, Miniature zero-backlash gears and actuators for precision positioning applications, Proc. 11th Eur. Sp. Mech. Tribol. Symp. - ESMATS 2005. (2005) 9–15.

[8] A.L. Greer, K.L. Rutherford, I.M. Hutchings, Wear resistance of amorphous alloys and related materials, Int. Mater. Rev. 47 (2002) 87–112. https://doi.org/10.1179/095066001225001067.

[9] A.L. Greer, Metallic glasses ... on the threshold, Mater. Today. 12 (2009) 14–22.

https://doi.org/10.1016/S1369-7021(09)70037-9.

[10] E. Fleury, S.M. Lee, H.S. Ahn, W.T. Kim, D.H. Kim, Tribological properties of bulk metallic glasses, Mater. Sci. Eng. A. 375–377 (2004) 276–279. https://doi.org/10.1016/j.msea.2003.10.065.

[11] Z. Parlar, M. Bakkal, A.J. Shih, Sliding tribological characteristics of Zr-based bulk metallic glass, Intermetallics. 16 (2008) 34–41. https://doi.org/10.1016/j.intermet.2007.07.011.

[12] B. Prakash, Abrasive wear behaviour of Fe , Co and Ni based metallic glasses, Wear. 258 (2005) 217–224. https://doi.org/10.1016/j.wear.2004.09.010.

[13] B.D.C. Hofmann, L.M. Andersen, J. Kolodziejska, S.N. Roberts, J. Borgonia, W.L. Johnson, K.S. Vecchio, A. Kennett, Optimizing Bulk Metallic Glasses for Robust , Highly Wear-Resistant Gears, Adv. Eng. Mater. 19 (2017) 1600541. https://doi.org/10.1002/adem.201600541.

[14] H.W. Jin, R. Ayer, J.Y. Koo, Reciprocating wear mechanisms in a Zr-based bulk metallic glass, J. Mater. Res. 22 (2007) 264–273. https://doi.org/10.1557/jmr.2007.0048.

[15] J. Kong, D. Xiong, J. Li, Q. Yuan, R. Tyagi, Effect of Flash Temperature on Tribological Properties of Bulk Metallic Glasses, Tribol. Lett. 35 (2009) 151–158. https://doi.org/10.1007/s11249-009-9444-4.

[16] S. Barlemont, P. Laffont, R. Daudin, A. Lenain, G. Colas, P. Cornuault, Strong dependency of the tribological behavior of CuZr-based bulk metallic glasses on relative humidity in ambient air, 11 (2023) 785–800.

[17] P.-H. Cornuault, G. Colas, A. Lenain, R. Daudin, S. Gravier, On the diversity of accommodation mechanisms in the tribology of Bulk Metallic Glasses, Tribol. Int. 141 (2020) 105957. https://doi.org/10.1016/j.triboint.2019.105957.

[18] S. Barlemont, G. Colas, A. Lenain, P. Cornuault, Effect of the countermaterial on the tribological behavior of Cu 45 Zr 46 Al 7 Nb 2 bulk metallic glass, Wear. (2023) 204712. https://doi.org/10.1016/j.wear.2023.204712.

[19] A. Caron, D. V. Louzguine-Luzguin, R. Bennewitz, Structure vs chemistry: Friction and wear of Pt-based metallic surfaces, ACS Appl. Mater. Interfaces. 5 (2013) 11341–11347. https://doi.org/10.1021/am403564a.

[20] D.C. Hofmann, R. Polit-casillas, S.N. Roberts, J. Borgonia, R.P. Dillon, E. Hilgemann, J. Kolodziejska, L. Montemayor, J. Suh, A. Hoff, K. Carpenter, A. Parness, W.L. Johnson, A. Kennett, B. Wilcox, Castable Bulk Metallic Glass Strain Wave Gears : Towards Decreasing the Cost of High-Performance Robotics, Sci. Rep. 6 (2016) 1–11. https://doi.org/10.1038/srep37773.

[21] G.C. Wood, T. Hodgkiess, The Hardness of Oxides at Ambient Temperatures, Mater. Corros. 23 (1972) 766–773. http://stacks.iop.org/0034-6683/1/i=3/a=I01.

[22] A. Caron, P. Sharma, A. Shluger, H.J. Fecht, D. V. Louzguine-Luzguin, A. Inoue, Effect of surface oxidation on the nm-scale wear behavior of a metallic glass, J. Appl. Phys. 109 (2011). https://doi.org/10.1063/1.3573778.

[23] A. Caron, C.L. Qin, L. Gu, S. González, A. Shluger, H.J. Fecht, D. V. Louzguine-Luzgin, A. Inoue, Structure and nano-mechanical characteristics of surface oxide layers on a metallic glass, Nanotechnology. 22 (2011). https://doi.org/10.1088/0957-4484/22/9/095704.

[24] S.B. Bukallah, M. Houalla, D.M. Hercules, Characterization of supported Nb catalysts by ToF-SIMS, Surf. Interface Anal. 29 (2000) 818–822. https://doi.org/10.1002/1096-9918(200012)29:12<818::AID-SIA931>3.0.CO;2-4.

[25] A. Priebe, T. Xie, G. Bürki, L. Pethö, J. Michler, The matrix effect in TOF-SIMS analysis of two-element inorganic thin films, J. Anal. At. Spectrom. 35 (2020) 1156–1166. https://doi.org/10.1039/c9ja00428a.

[26] E. Djurado, P. Bouvier, G. Lucazeau, Crystallite size effect on the tetragonal-monoclinic transition of undoped nanocrystalline zirconia studied by XRD and Raman spectrometry, J. Solid State Chem. 149 (2000) 399–407. https://doi.org/10.1006/jssc.1999.8565.

[27] J. Kim, K.J. Choi, C.B. Bahn, J.H. Kim, In situ Raman spectroscopic analysis of surface oxide films on Ni-base alloy/low alloy steel dissimilar metal weld interfaces in high-temperature water, J. Nucl. Mater. 449 (2014) 181–187. https://doi.org/10.1016/j.jnucmat.2014.03.038.

[28] G. Falk, M. Borlaf, M.J. López-Muñoz, J.C. Fariñas, J.B. Rodrigues Neto, R. Moreno, Microwave-assisted synthesis of Nb2O5 for photocatalytic application of nanopowders and thin films, J. Mater. Res. 32 (2017) 3271–3278. https://doi.org/10.1557/jmr.2017.93.

[29] L.K.S. Herval, D. Von Dreifus, A.C. Rabelo, A.D. Rodrigues, E.C. Pereira, Y.G. Gobato, A.J.A. De Oliveira, M.P.F. De Godoy, The role of defects on the structural and magnetic properties of Nb2O5, J. Alloys Compd. 653 (2015) 358–362. https://doi.org/10.1016/j.jallcom.2015.09.019.

[30] J. Santander, E. López, A. Diez, M. Dennehy, M. Pedernera, G. Tonetto, Ni-Nb mixed oxides: One-pot synthesis and catalytic activity for oxidative dehydrogenation of ethane, Chem. Eng. J. 255 (2014) 185–194. https://doi.org/10.1016/j.cej.2014.06.048.

[31] A.M. Jubb, H.C. Allen, Vibrational spectroscopic characterization of hematite, maghemite, and magnetite thin films produced by vapor deposition, ACS Appl. Mater. Interfaces. 2 (2010) 2804–2812. https://doi.org/10.1021/am1004943.

[32] E. Husson, Y. Repelin, N.Q. Dao, H. Brusset, Normal coordinate analysis of the MNb2O6 series of columbite structure (M = Mg, Ca, Mn, Fe, Co, Ni, Cu, Zn, Cd), J. Chem. Phys. 67 (1977) 1157–1163. https://doi.org/10.1063/1.434968.

[33] Y. De Luna, N. Bensalah, Mechanochemical Synthesis of Orthorhombic Nickel Niobate (NiNb2O6) as a Robust and Fast Charging Anode Material for Lithium-Ion Batteries, ACS Appl. Energy Mater. 5 (2022) 7443–7457. https://doi.org/https://doi.org/10.1021/acsaem.2c00935.

[34] T. Sri Devi Kumari, R. Vinith Gandhi, G. Rahul, G. Kamalanathan, T. Prem Kumar, D. Jeyakumar, N. Lakshminarasimhan, Electrochemical lithium insertion behavior of FeNbO4: Structural relations and in situ conversion into FeNb2O6 during carbon coating, Mater. Chem. Phys. 145 (2014) 425–433. https://doi.org/10.1016/j.matchemphys.2014.02.031.

[35] R. Babu, S. Kelkar, V. Kashid, S.N. Achary, H.G. Salunke, N.M. Gupta, Photophysical, bandstructural, and textural properties of o-FeNbO 4 in relation to its cocatalyst-assisted photoactivity for water oxidation, RSC Adv. 4 (2014) 33435–33445. https://doi.org/10.1039/c4ra06059h.

[36] S. Devesa, M.P. Graça, F. Henry, L.C. Costa, Dielectric properties of FeNbO4 ceramics prepared by the sol-gel method, Solid State Sci. 61 (2016) 44–50. https://doi.org/10.1016/j.solidstatesciences.2016.09.005.

[37] N. Ballarini, G. Calestani, R. Catani, F. Cavani, U. Cornaro, C. Cortelli, M. Ferrari, Oxide Based Materials - New sources, novel phases, new applications, Stud. Surf. Sci. Catal. 155 (2005) 81–94. http://www.sciencedirect.com/science/article/pii/S0167299105801399.

[38] W. Jiang, M. Li, J. Sha, C. Zhou, Microstructure and oxidation resistance of composition gradients Nb-Si based alloy thin film, Mater. Des. 192 (2020) 108687. https://doi.org/10.1016/j.matdes.2020.108687.

[39] R.M. Pittman, A.T. Bell, Raman studies of the structure of Nb2O5/TiO2, J. Phys. Chem. 97 (1993) 12178–12185. https://doi.org/10.1021/j100149a013.

[40] T. Ikeya, M. Senna, Change in the structure of niobium pentoxide due to mechanical and thermal treatments, J. Non. Cryst. Solids. 105 (1988) 243–250. https://doi.org/10.1016/0022-3093(88)90313-4.

[41] J.M. Jehng, I.E. Wachs, Structural Chemistry and Raman Spectra of Niobium Oxides, Chem. Mater. 3 (1991) 100–107. https://doi.org/10.1021/cm00013a025.

[42] J.E. Maslar, W.S. Hurst, W.J. Bowers, J.H. Hendricks, M.I. Aquino, I. Levin, In situ Raman spectroscopic investigation of chromium surfaces under hydrothermal conditions, Appl. Surf. Sci. 180 (2001) 102–118. https://doi.org/10.1016/S0169-4332(01)00338-5.

[43] J.E. Maslar, W.S. Hurst, T.A. Vanderah, I. Levin, The Raman Spectra of Cr3O8 and Cr2O5, J. Raman Spectrosc. 32 (2001) 201–206. https://doi.org/10.1002/jrs.687.

[44] S.R. Chowdhury, E.K. Yanful, A.R. Pratt, Chemical states in XPS and Raman analysis during removal of Cr(VI) from contaminated water by mixed maghemite-magnetite nanoparticles, J. Hazard. Mater. 235–236 (2012) 246–256. https://doi.org/10.1016/j.jhazmat.2012.07.054.

[45] J.E. Maslar, W.S. Hurst, W.J. Bowers, J.H. Hendricks, E.S. Windsor, Alloy 600 Aqueous Corrosion at Elevated Temperatures and Pressures: An In Situ Raman Spectroscopic Investigation, J. Electrochem. Soc. 156 (2009) C103. https://doi.org/10.1149/1.3056038.

[46] Y. Yu, F. He, Z. Qiao, Z. Wang, W. Liu, J. Yang, Effects of temperature and microstructure on the triblogical properties of CoCrFeNiNbx eutectic high entropy alloys, J. Alloys Compd. 775 (2019) 1376–1385. https://doi.org/10.1016/j.jallcom.2018.10.138.

[47] D.P. Weston, P.H. Shipway, S.J. Harris, M.K. Cheng, Friction and sliding wear behaviour of electrodeposited cobalt and cobalt-tungsten alloy coatings for replacement of electrodeposited

chromium, Wear. 267 (2009) 934–943. https://doi.org/10.1016/j.wear.2009.01.006.

[48] A. Amanov, S. Sasaki, I.S. Cho, Y. Suzuki, H.J. Kim, D.E. Kim, An investigation of the tribological and nano-scratch behaviors of Fe-Ni-Cr alloy sintered by direct metal laser sintering, Mater. Des. 47 (2013) 386–394. https://doi.org/10.1016/j.matdes.2012.11.062.

[49] J.H. Hsieh, C. Li, A.L.K. Tan, C.K. Poh, N.J. Tan, Study of oxidation and wear behaviors of (Nb,Cr)N thin films using Raman spectroscopy, Surf. Coatings Technol. 177–178 (2004) 299–305. https://doi.org/10.1016/j.surfcoat.2003.09.008.